Original Article

Experimental and theoretical insights to demonstrate the hydrogen evolution activity of layered platinum dichalcogenides electrocatalysts

Check for updates

Sajjad Hussain [a,b], *Kamran Akbar* [c], *Dhanasekaran Vikraman* [d], *Iqra Rabani* [b], *Wooseok Song* [e], *Ki-Seok An* [e], *Hyun-Seok Kim* [d], *Seung-Hyun Chun* [f], *Jongwan Jung* [a,b,*]

[a] *Hybrid Materials Center (HMC), Sejong University, Seoul 05006, Republic of Korea*
[b] *Department of Nanotechnology and Advanced Materials Engineering, Sejong University, Seoul 05006, Republic of Korea*
[c] *Department of Molecular Sciences and Nanosystems, Ca' Foscari Unversity of Venice, Via Torino 155, 30172, Venezia Mestre, Italy*
[d] *Division of Electronics and Electrical Engineering, Dongguk University-Seoul, Seoul 04620, Republic of Korea*
[e] *Thin Film Materials Research Center, Korea Research Institute of Chemical Technology, Daejeon 34114, Republic of Korea*
[f] *Department of Physics, Sejong University, Seoul 05006, Republic of Korea*

ARTICLE INFO

ABSTRACT

Hydrogen is a highly efficient and clean renewable energy source and water splitting through electrocatalytic hydrogen evolution is a most promising approach for hydrogen generation. Layered transition metal dichalcogenides-based nano-structures have recently attracted significant interest as robust and durable catalysts for hydrogen evolution. We systematically investigated the platinum (Pt) based dichalcogenides (PtS_2, $PtSe_2$ and $PtTe_2$) as highly energetic and robust hydrogen evolution electrocatalysts. $PtTe_2$ catalyst unveiled the rapid hydrogen evolution process with the low overpotentials of 75 and 92 mV (vs. RHE) at a current density of 10 mA cm^{-2}, and the small Tafel slopes of 64 and 59 mV/dec in acidic and alkaline medium, respectively. The fabricated $PtTe_2$ electrocatalyst explored a better catalytic activity than PtS_2 and $PtSe_2$. The density functional theory estimations explored that the observed small Gibbs free energy for H-adsorption of $PtTe_2$ was given the prominent role to achieve the superior electrocatalytic and excellent stability activity towards hydrogen evolution due to a smaller bandgap and the metallic nature. We believe that this work will offer a key path to use Pt based dichalcogenides for hydrogen evolution electrocatalysts.

* Corresponding author.
E-mail address: jwjung@sejong.ac.kr (J. Jung).

1. Introduction

Hydrogen production is a highly efficient, secure, and clean renewable energy source that could replace traditional fossil fuels in the future, because of its impressive energy density, zero carbon emissions, and environmental friendliness [1,2]. Electrocatalytic hydrogen evolution reaction (HER) is one of the most promising approaches for hydrogen generation from water splitting [3—5]. The various two dimensional materials and nanostructures including MXene and its hybrid composites, black phosphorus, metal nitrides and carbides, metal composites, transition metal dichalcogenides (TMDs) and graphene based derivatives were extensively studied due to their excellent physical and chemical properties such as abundant surface groups, strong electrical conductivity, larger interlayer spacing between the layer, easily tunable structure and sp^3 hybridization behavior for the electro- and photo-catalytic applications [6—13]. Amongst, TMDs are being paid a lot of attention as a promising systems for HER due to their high abundance, low cost, high conductivity, superior electronic arrangements, and excellent catalytic peculiarities [3,14,15]. Most of them produced the inferior HER properties in an acidic or alkaline medium. Therefore, to unearth new systems as electrocatalysts with high HER abilities are energetically being pursued [16]. Platinum (Pt) electrodes are being used as successful commercial HER electrocatalysts thus far with superior electrocatalytic behavior. However, their scarcity and high costs have constrained their uses in industrials. Hence, the derivatives of Pt can undoubtedly have a high Pt like catalytic behavior, and their properties can be tuned with the bond of desirable atoms.

Pt based dichalcogenides, which include PtS_2, $PtSe_2$, and $PtTe_2$, are emerging materials, and they can be easily thinned to the ultimate dimension of a single layer even the exfoliated ones. From the literatures and the theoretical perceptions, PtS_2 is a semiconductor with an energy gap of about 1.2 eV [17]. $PtTe_2$ is supposed to be a metal, and $PtSe_2$ is considered to be a semi-metal with a zero bandgap [18]. However, the recent experimental studies demonstrated that monolayer $PtSe_2$ has bandgap of 1.2 eV with higher carrier mobility, which suggests the possibility to operate as a semiconductor and a semimetal [19]. Wang et al. [20] have successfully adopted a single step epitaxial methodology with a direct selenization on Pt (111) substrate to obtain a monolayer $PtSe_2$. Zeng et al. [21] also employed the above methodology to grow large-scale, uniform, and vertical $PtSe_2$ films. Because of a unique crystal structure, the excellent surface characteristics, and the abundance of active sites on the exposed surfaces, Pt based dichalcogenides have been received considerable attention as a superior electrocatalysts which can possible to catalyze the couple of electrons and protons as H_2 at the maximum rate of reaction with low overpotentials [22].

Despite significant successes, immense research has been conducting to design the efficient HER catalysts [13,18,23,24]. The immense efforts have been done by our group to produce the transition metal dichalcogenides based electrocatalysts using the various physical and chemical methodologies [25—27]. Recently, Pt based dichalcogenides were fabricated with different chalcogen (S, Se, and Te) atoms to promote electrocatalytic activities [15,28]. Chia et al. [15] have reported PtS_2, $PtSe_2$, and $PtTe_2$ as hydrogen-evolving electrodes with the featured overpotentials of 86, 63, and 54 mV at a 10 $mAcm^{-2}$ current density and the Tafel slopes of 216, 132, and 110 mV/dec, respectively, which harmoniously focus the Pt derivatives as an alternative to pure Pt. Rosli et al. [29] also proposed Pt derivatives, which included PtS_2, $PtSe_2$, and $PtTe_2$, as the electrocatalyst materials for an oxygen reduction reaction. Recently, a 1 T-$PtSe_2$ thin film was synthesized by the chemical vapor deposition (CVD) on Au foil as a HER electrocatalyst which produced the overpotentials ~210—261 mV to drive a 10 $mAcm^{-2}$ current density and Tafel slopes of ~33—38 mV/dec [30].

Based on the detailed literatures, we have the prominent interest to substitute the chalcogen atom with Pt to derive the novel characteristic structure in order to perceive the superior electrocatalytic properties. Hence, the two step preparation process of sputtering and CVD annealing were used to construct the PtS_2, $PtSe_2$, and the $PtTe_2$ thin films on the Ti/Si substrate. The prepared $PtTe_2$ electrocatalysts show highly effective and stable activity in an acidic and alkaline electrolyte for HER, showing low overpotentials (75 & 92 mV @10 mA cm^{-2}) and the small Tafel slopes (64 & 59 mV/dec). The catalytic activity of $PtTe_2$ is superior to other electrocatalysts including PtS_2 and $PtSe_2$. The density functional theory (DFT) approximations were also used to measure the valuable theoretical insights and the Gibbs free energy of adsorption for hydrogen (ΔG_H*) of Pt derivatives demonstrating their excellent HER properties. The observed experimental results are highly concurred with the theoretical predictions.

2. Materials and methods

2.1. Synthesis of Pt-dichalcogenides

The Si substrates were first ultrasonically cleaned by using methanol, acetone, and isopropyl alcohol solutions. The ultrasonically cleansed substrates were dressed using deionized water and then dehydrated and baked for 5 min. The size of the substrates was 1×1 cm^{-1}. Before the film preparation, the sputter chamber was evacuated by using the combined diffusion pump and rotary pump to attain a vacuum of 1×10^{-6} Pa. Initially, a seed layer of Ti (3~5 nm) film was coated using RF magnetron sputtering at room temperature. For Ti layer deposition, working pressure (~3×10^{-2} torr), Ar gas flow (10 sccm), power (25 W), and sputtering time (200 s) were fixed constantly. The active layer of PtS_2, $PtSe_2$, and $PtTe_2$ were grown using two-step processes. In the first step, thin Pt (10 nm) film was developed using RF magnetron sputtering at room temperature. For Pt film sputtering, the constant sputtering time (400 s), working pressure (~3×10^{-2} torr), power (50 W) and Ar gas flow (10 sccm) were used. In the second step, the Pt/Ti/Si film was placed to oven to anneal at 650 °C in the presence of S or Se or Te powder using Ar/H_2 (50/10 sccm) environment for 1 h to form PtS_2, $PtSe_2$ or $PtTe_2$, respectively. To make the S, Se or Te environment, the constant weight of chalcogenide (0.4 g for S/Se/Te powder) and the distance between the boat and substrate (~50 mm) were used. The

detailed characterization and computational parts are provided in the supporting information.

2.2.   *Electrochemical measurements*

Electrochemical measurements were performed using a Bio-logic SP-300 workstation with a standard three-electrode system. The commercial Pt/C and synthesized PtS_2, $PtSe_2$, and $PtTe_2$ were employed as the working electrodes without additional treatment with a graphite rod as a counter electrode. A saturated calomel electrode (SCE) for acidic media and an Hg/HgO electrode for alkaline media were employed as a reference electrode in a three-electrode system. The linear sweep polarization measurement (scan rate of 10 mV/s) was conducted in a nitrogen purged 0.5 M H_2SO_4 and 1.0 M KOH electrolyte. All data were corrected from the iR losses and the background current during the measurement. The HER potential values for reversible hydrogen electrode (RHE) were transformed by the formula: E (vs RHE) = E (vs SCE) + E^0 (SCE) + 0.0592 × pH for H_2SO_4 medium and E (vs RHE) = E (vs Hg/HgO) + E^0 (Hg/HgO) + 0.0592 × pH for KOH medium. Cyclic voltammograms (CVs) were cycled in the non-Faradic region under various scan rates from 10 to 100 mVs^{-1} in the acidic medium. The EIS tests were engaged at frequencies ranging from 10 mHz to 1 MHz.

3.   Results and discussion

PtS_2, $PtSe_2$, and $PtTe_2$ electrodes were prepared by RF magnetron sputtering-CVD methods (Fig. 1). The complete experimental details are provided in the materials and the methods section. Briefly, the sputtered Pt-substrates were annealed in the presence of S, Se, and Te to form PtS_2, $PtSe_2$, and $PtTe_2$, respectively. To discover the structural property of the prepared PtS_2, $PtSe_2$, and $PtTe_2$ films, the Raman analyses

were examined (Fig. 2a). For the PtS_2 film, a couple of characteristic peaks are exhibited at ~306.5 and ~ 336.1 cm^{-1} due to the in-plane mode E^1_g and the out-of-plane mode A^1_g, respectively [31,32]. In the case of $PtSe_2$, two prominent vibrational modes appeared at ~175.8 and ~205.7 cm^{-1}, which are allocated to the in-plane E^1_g and the out-of-plane A^1_g, respectively, which is consistent with the previous report [33]. From $PtTe_2$, the representative peaks are at ~109.6 and ~157.4 cm^{-1} correspond to the E^1_g and A^1_g longitudinal acoustic phonon modes due to the existence of 1 T-$PtTe_2$ [34,35]. Furthermore, the X-ray diffraction (XRD) studies were used to confirm the crystal structure of PtS_2, $PtSe_2$, and $PtTe_2$ as shown in Fig. 2b. PtS_2 is exposed the (001) (100) (011) (012) (110), and (111) lattice planes (JCPDS No. 88—2267), while the strong peak related to the Si (100) plane are exhibited. For $PtSe_2$, the (001) (100) (011) (102) (110), and (201) planes are observed (JCPDS No. 89—2643) along with the Si peak. In the case of $PtTe_2$ (001) (011) (002) (102) (110) (111) (003) (201) (103), and (022) lattice planes are observed (JCPDS No. 88—2277). Hence, the observed structural characterizations strongly proved the formation of PtS_2, $PtSe_2$, and $PtTe_2$ evidently.

To prove the electronic structure of the synthetic PtS_2, $PtSe_2$, and $PtTe_2$ film, an X-ray photoemission spectroscopy (XPS) was performed (Fig. 3). The survey spectrum for PtS_2, $PtSe_2$, and $PtTe_2$ films are provided in Fig. S1, which clearly picturized the observed elements. For PtS_2, the strong Pt 4f doublets are centered at 76.4 eV and 73.1 eV attributed to Pt $4f_{5/2}$ and Pt $4f_{7/2}$, respectively (Fig. 3a) [36]. Also, S $2p_{1/2}$ and S $2p_{3/2}$ are centered at 164.0 eV and 162.7 eV, respectively (Fig. 3b) [28]. The $PtSe_2$ film (Fig. 3c-d) is produced the Pt 4f doublets at 76.6 eV (Pt $4f_{5/2}$) and 73.3 eV (Pt $4f_{7/2}$), whereas Se 3 d doublets are at 55.7 (Se $3d_{3/2}$) and 54.7 eV (Se $3d_{5/2}$), which is consistent with the reported values for $PtSe_2$ [21,37]. For the $PtTe_2$ film (Fig. 3e-f), the characteristic Pt 4f doublets are exhibited at 76.9 eV (Pt $4f_{5/2}$) and 73.6 eV (Pt $4f_{7/2}$). And Te 3 d signals are at 584.1 and 573.6 eV correspond to the $3d_{3/2}$ and
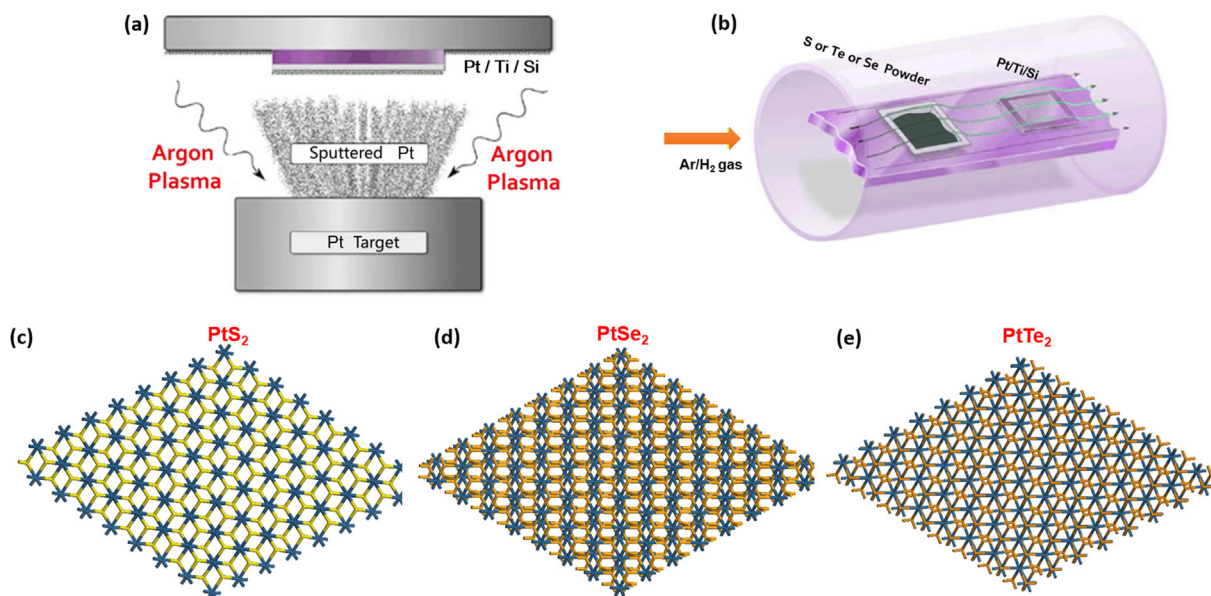

Fig. 1 — (a) RF sputtering to deposit on Pt on Ti/Si; (b) CVD annealing to form Pt-chalcogenides; their chemical structure (c) PtS_2, (d) $PtSe_2$, and (e) $PtTe_2$.
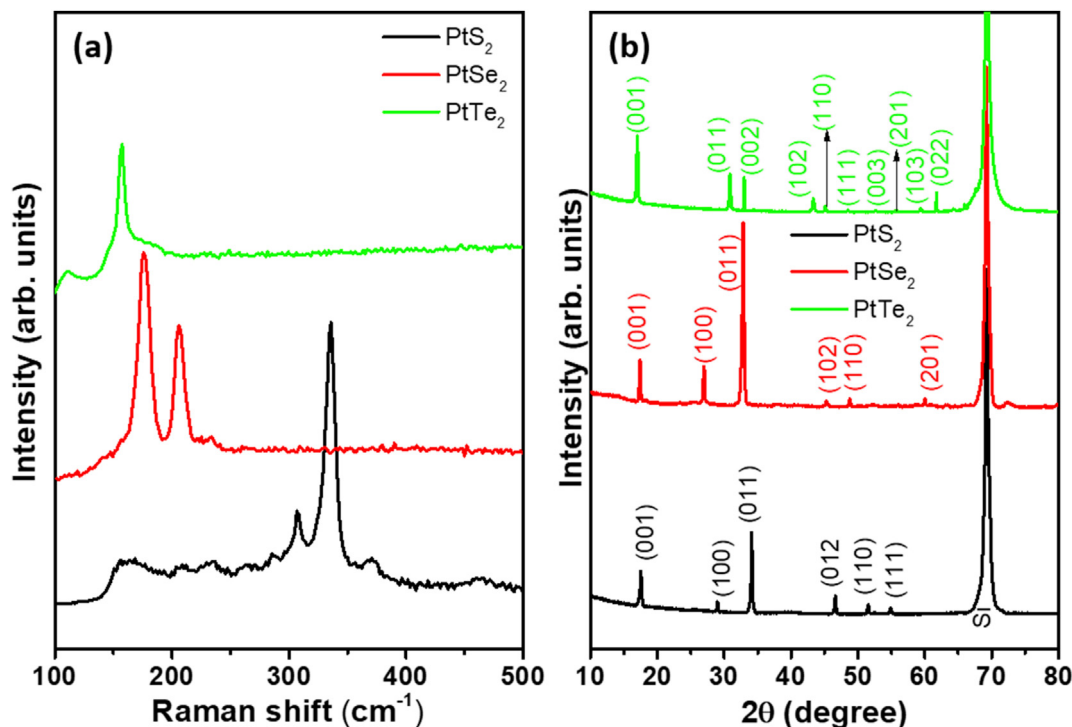
Fig. 2 — (a) Raman spectra and (b) XRD patterns of PtS_2, $PtSe_2$, and $PtTe_2$.

$3d_{5/2}$ binding energies, respectively, along with the Te^{4+} peaks (587.1 and 576.9 eV) [28,38].

Surface properties are crucial to determine the catalytic properties of PtS_2, $PtSe_2$, and $PtTe_2$. Hence, field emission scanning electron microscope (FESEM) and transmission electron microscopy (TEM) studies were carried out. Fig. 4 shows the FESEM and the TEM images of PtS_2 with different magnifications. The nano-cluster like morphological nature is exhibited for PtS_2, which clearly depicted in Fig. 4a-b. The high resolution FESEM image (Fig. 4c) reveals the formation of grain bunches by agglomeration. The nano-strip like structured fringes are exposed by the TEM images, which are given in Fig. 4d-f. The high resolution images (Fig. 4g-h) are clearly picturized, and their zoomed portion of the selected region are inserted (inset Fig. 4g-h). The fast Fourier transform (FFT) pattern, which was derived from Fig. 4h and their inverse FFT (iFFT) pattern are given in Fig. 4i-j, respectively. The phase profile spectrum for the iFFT pattern is exhibited with 0.51 nm corresponding to the (001) lattice orientation of PtS_2 which is correlated with XRD result.

The acquired FESEM and TEM images for the $PtSe_2$ with different magnifications are provided in Fig. 5. The highly interconnected cauliflower structured grains are exhibited for the $PtSe_2$ as shown in Fig. 5a-b. The strained spherical shaped grain bunches by agglomeration of smaller grains are grouped on the $PtSe_2$ surface. Figure 5c displays the cauliflower natured grain bunches effectively due to the formation of more active selenium facet sites for the $PtSe_2$. The different shape of the grains bunches is clearly marked by the TEM images with the inset of corresponding high magnification images (Fig. 5d-f). The high resolution images are clearly visualized by the shape of the nano-stripe structured grains

with a FFT pattern (Fig. 5g). The different directions of nano-stripe structured fringes are captured by the high resolution image, and their (011) and (100) lattice orientations are indexed by the blue and yellow line, respectively. FFT pattern (Fig. 5i) is mapped for the selected spot of lattice directions. The iFFTs and phase profile spectra of (011) and (100) lattice orientations of $PtSe_2$ are given in Fig. 5j-m, which demonstrated the existence of nano-stripe structures with the interconnection of different lattices for $PtSe_2$.

Fig. 6 shows the FESEM and the TEM images for the metallic natured $PtTe_2$. The lower magnification image clearly predicts the dense nature morphology (Fig. 6a). The high resolution images proved the group of grain clusters with plenty of active sites in a multi-directed grain formation. The uniform surface nature with a homogeneous texture of grains with confined directions are validated in Fig. 6c. Fig. 6d shows the TEM image with the vertically aligned nano-strip structure for the $PtTe_2$ with an FFT pattern. The vertically aligned nano-strip structures are clearly discovered by the high resolution TEM (Fig. 6e-f). The width of the strip bands and their directions varied due to their different lattice directions. Inset Fig. 6f shows the FFT pattern for the red color selected portion in Fig. 6f. The highly patterned nano-stripes with lattice intersections are revealed in the high resolution TEM image of Fig. 6g-h with the inset FFT patterns. The different directions of nano-stripes for the selected part zoomed images are provided within the circle for the arrowed region of Fig. 6g-h. The extracted phase profile spectrum with spacing of 0.29 nm reveals the (011) lattice orientation of $PtTe_2$ (Fig. 6i). Furthermore, to prove the existence of the Pt-dichalcogenides, an energy-dispersive X-ray spectrum measurements were used for PtS_2, $PtSe_2$, and $PtTe_2$ (Figs. S2a—c). The observed elemental
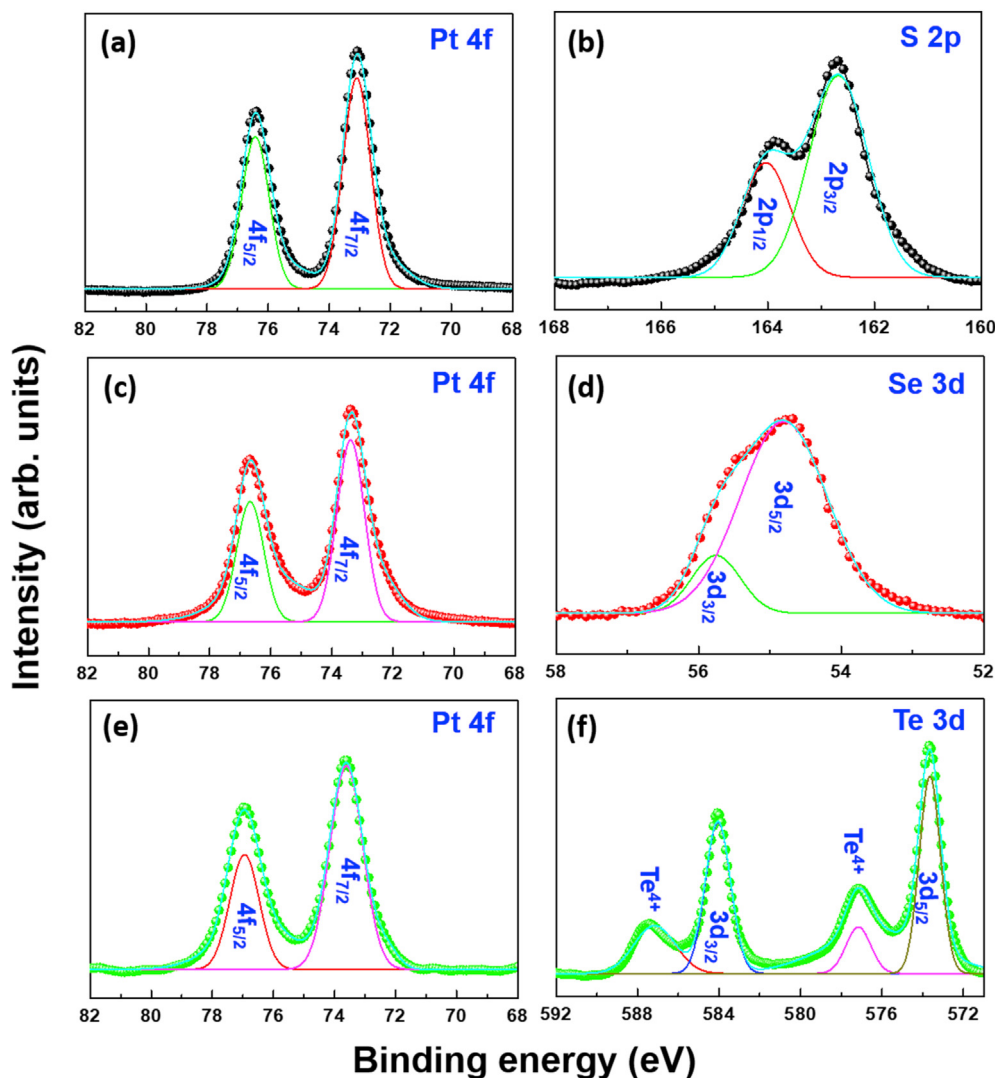
Fig. 3 — XPS studies of PtS_2, $PtSe_2$ and $PtTe_2$. Binding energy spectra of (a) Pt 4f, (b) S 2p for PtS_2; Binding energy spectra of (c) Pt 4f, (d) Se 3 d for $PtSe_2$ and Binding energy spectra of (e) Pt 4f, (f) Te 3 d for $PtTe_2$.

ratios are 68:32 (S:Pt), 65:35 (Se:Pt) and 71:29 (Te:Pt) for PtS_2, $PtSe_2$, and $PtTe_2$, respectively. Also, the elemental mapping images by SEM and TEM analyses for PtS_2, $PtSe_2$, and $PtTe_2$ to validate the existence of the suggested elements are provided in Figs. S3 and S4, respectively.

The electrocatalytic measurements towards HER using Pt-dichalcogenides as the electrocatalysts were assessed through the conventional three electrode set-up in an N_2 purged 0.5 M H_2SO_4 medium with a scan rate of 10 mV s^{-1}. Fig. 7a andb shows the linear sweep voltammetry (LSV) curves for the commercial Pt/C and the Pt-chalcogenide PtS_2, $PtSe_2$, and $PtTe_2$ electrocatalysts. The commercial Pt/C catalyst shows high HER catalytic performance with an overpotential of 43 mV @10 mA cm^{-2} in H_2SO_4 medium. Remarkably, the $PtTe_2$ electrode exhibited superior HER activity in H_2SO_4 medium with the lowest overpotential of 75 mV to drive 10 mA cm^{-2}, which is comparable to that of commercial Pt/C. On the other hand, the PtS_2 and the $PtSe_2$ showed slightly inferior HER activity compared with the $PtTe_2$ (92 mV and

81 mV at 10 mA cm^{-2}, respectively, in H_2SO_4 medium). The observed overpotentials for the different electrocatalysts are listed in Table 1. The observed low overpotential of $PtTe_2$ is credited to the metallic nature of the system. The exhibited $PtTe_2$ based electrode HER result is also much more superior than those of the various LTMDs based catalysts, such as $Ni_{0.89}Co_{0.11}Se_2$ MNSN/NF ($\eta_{10mAcm}^{-2} = 85$ m V) [4], $MoS_2/CoSe_2$ hybrid ($\eta_{1-10mAcm}^{-2} = 11–68$ mV) [39], MoSSe@rGO nano-composites ($\eta_{5mAcm}^{-2} = 135$ m V) [40], WSe_2/MoS_2 ($\eta_{10mAcm}^{-2} = 116$ mV) [23], edge-oriented $WS_{2(1-x)}Se_{2x}$ on 3D porous $NiSe_2$ foam [41], $WS_{2(1-x)}Se_{2x}$ nanoribbons ($\eta_{10mAcm}^{-2} = 170$ m V) [42], $MoS_{2(1-x)}Se_{2x}/NiSe_2$ hybrid ($\eta_{10mAcm}^{-2} = 69$ mV) [43], $WS_{1-x}Se_x$ ($\eta_{10mAcm}^{-2} = 93$ mV) [44], $WS_2/CoSe_2$ ($\eta_{10mAcm}^{-2} = 95$ mV) [45], $NiP_{1.93}Se_{0.07}$ and $NiP_{0.09}Se_{1.91}$ heterostructures ($\eta_{10mAcm}^{-2} = 84–135$ m V) [46], MoS_2 heterogeneous-phase nanosheets ($\eta_{10mAcm}^{-2} = 220$ m V) [47], 2H- and 1 T′-$MoTe_2$ single crystals ($\eta_{10mAcm}^{-2} = 650$ & 356 m V) [48], porous $NiTe_2$ nanostructures ($\eta_{10mAcm}^{-2} = -422$ mV) [49], and porous hollow NiS_2 microspheres ($\eta_{10mAcm}^{-2} = 174$ m V)
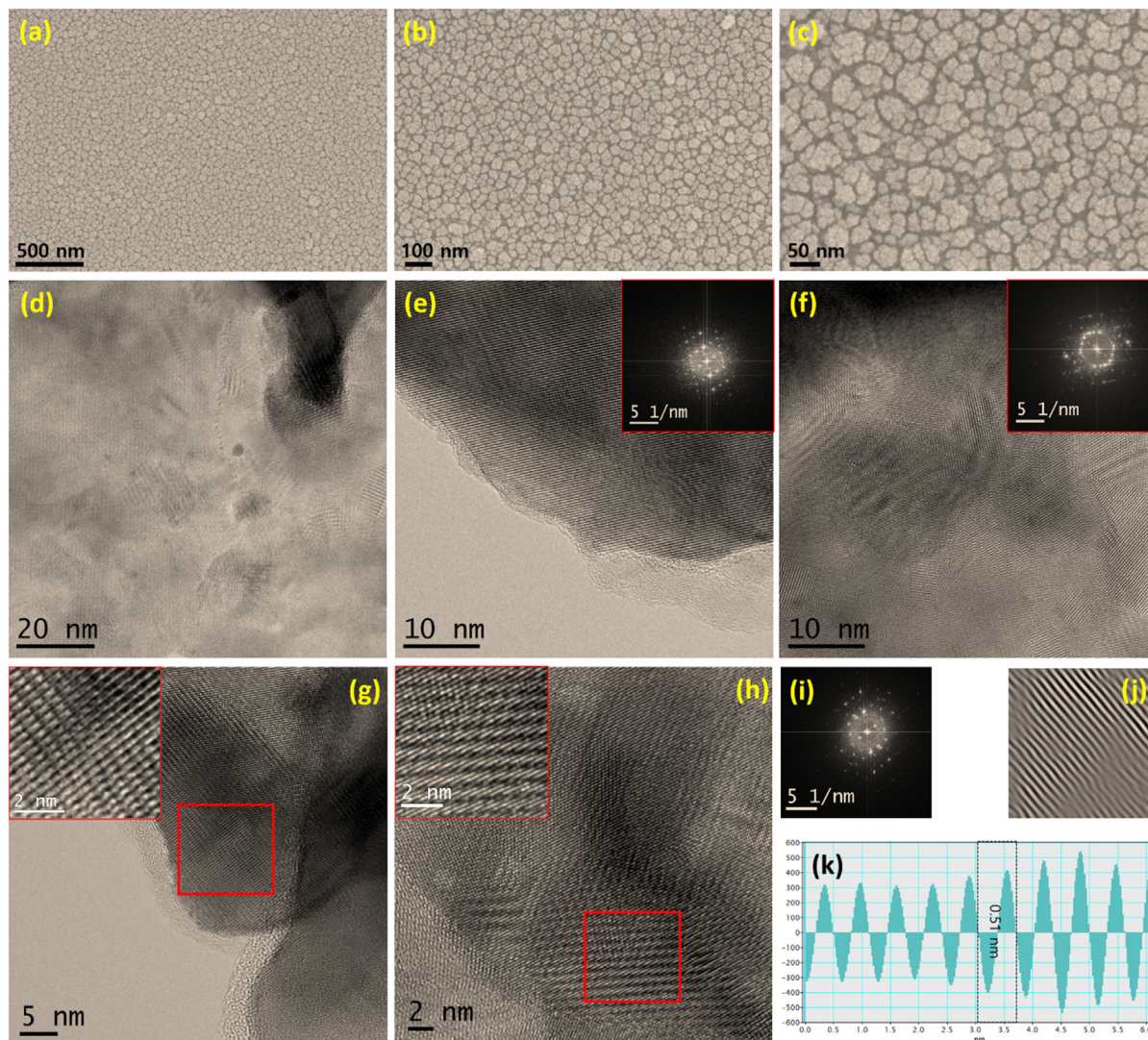
Fig. 4 − Morphological studies of PtS₂ (a−c) Low and high magnification FESEM images (d−f) Low and higher magnification TEM images with the inset of FFT pattern (g−h) High resolution TEM image with nano-stripe structured fringes in the inset for red color selected portions in the corresponding image; (i) FFT pattern and (j) inverse FFT by point mask mode (k) phase profile spectrum with 0.51 nm spacing related to PtS₂ 001 lattice orientation.

[50]. The extracted overpotential value of the PtTe₂ is elaborately compared to various LTMDs based HER catalysts in Table S1.

The Tafel plots provide more valuable insights of the electrocatalysts. Fig. 7c shows the Tafel plots for the Pt/C, PtS₂, PtSe₂, and the PtTe₂ electrodes, which were extracted from their relevant polarization curves in H₂SO₄ medium. The Tafel slopes were extracted from the fitted lines for each of the electrodes. PtTe₂ electrode owns a lesser Tafel slope of 64 mV/dec than that of the PtSe₂ (71 mV/dec) and the PtS₂ (69 mV/
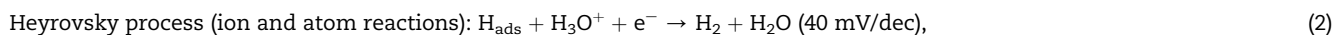
dec). Also, the commercial Pt/C electrode exhibits the 42 mV/dec of Tafel slope in H₂SO₄ medium. By extrapolating the Tafel plot to the X-axis, the additional inherent HER activity, the exchange current density (j_0) of the catalyst was extracted for H₂SO₄ medium. The assessed j_0 values are 1.31, 0.65, 0.73, and 0.77 mA cm^{-2} for the Pt/C, PtS₂, PtSe₂, and the PtTe₂, respectively. The observed Tafel slope and j_0 values are provided in Table 1. Three primary steps in the hydrogen evolution process using acidic electrolyte follows, [44,51,52].

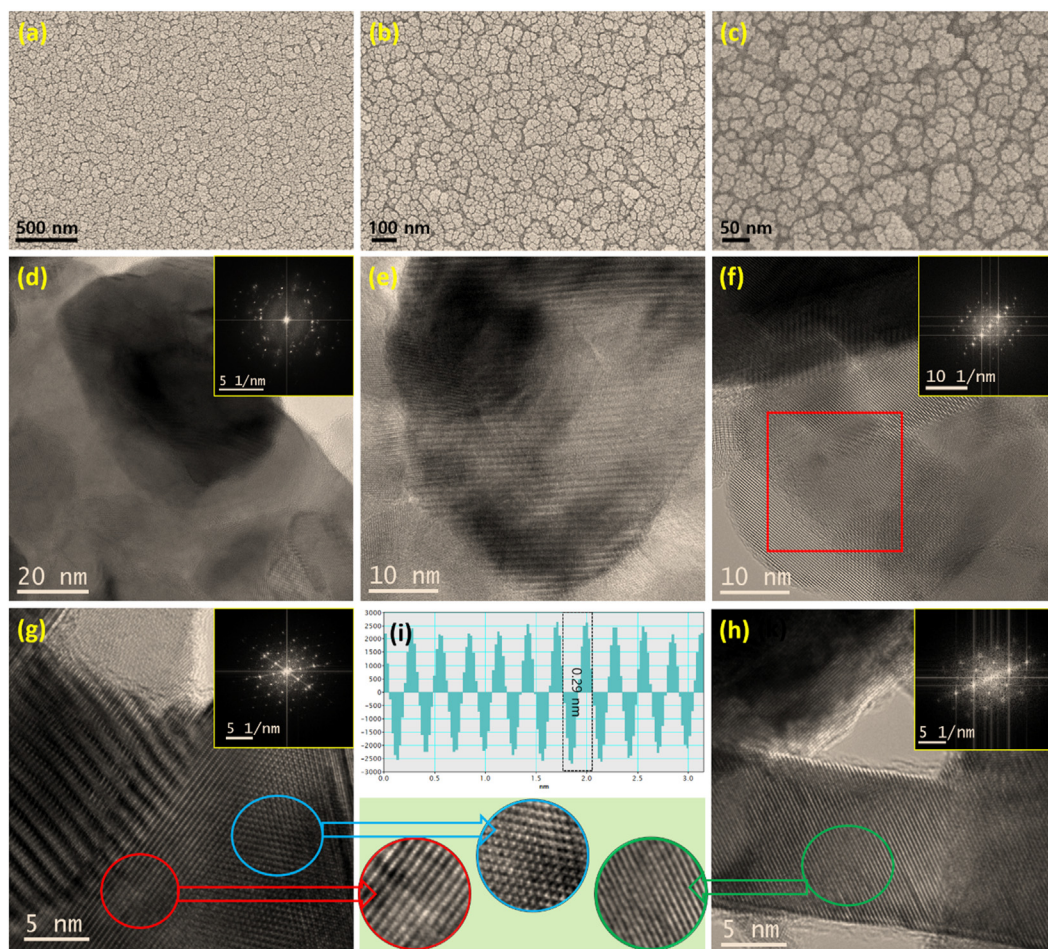Volmer step (discharge reaction): $H_3O^+ + e^- \rightarrow H_{ads} + H_2O$ (120 mV/dec),   (1)
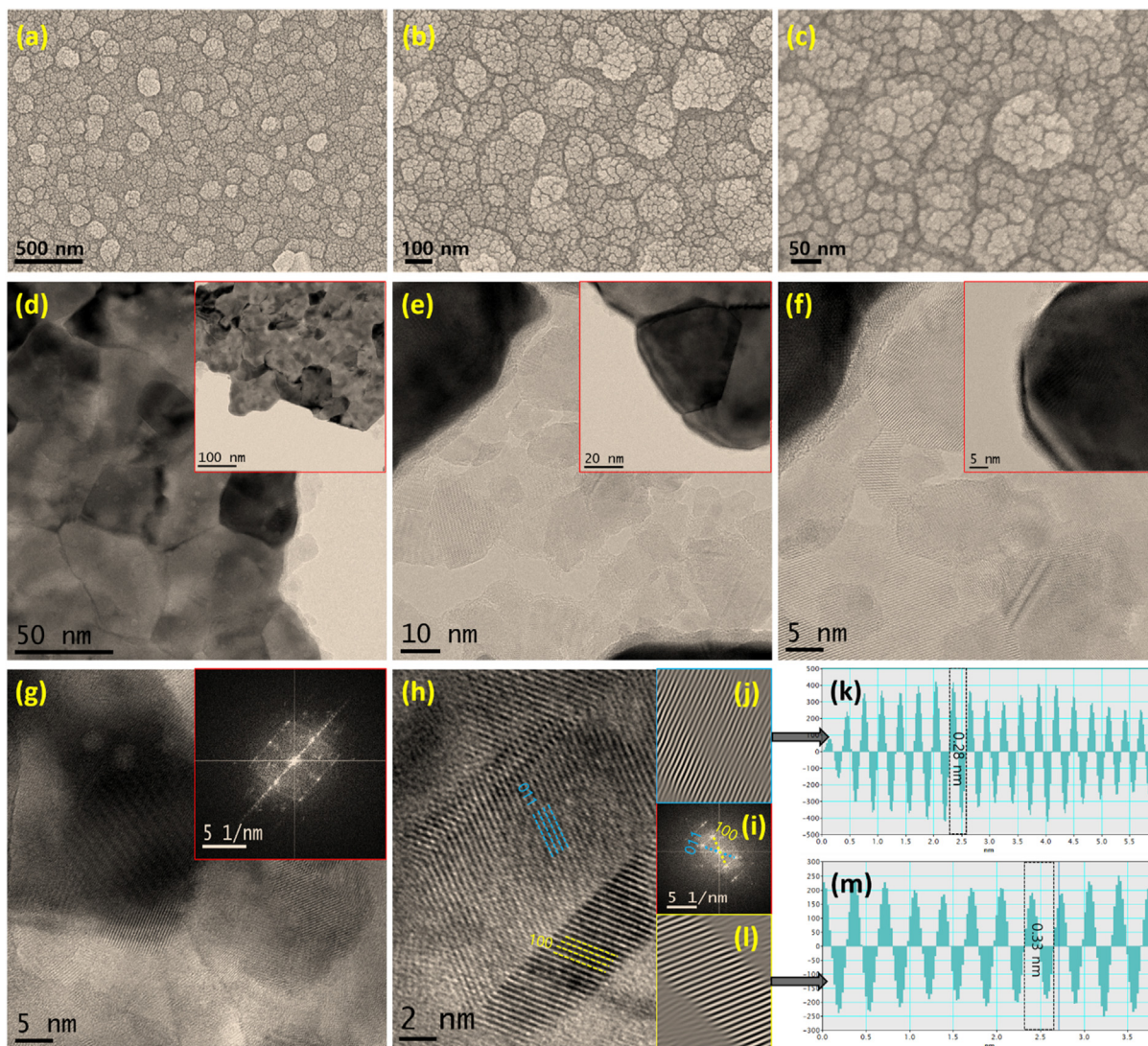
Fig. 5 − Morphological studies of PtSe₂ (a−c) Low and high magnification FESEM images (d−f) Low and higher magnification TEM images; (g) High resolution TEM image (inset − FFT pattern); (h) Nano-stripe structured fringes with 011 and 100 lattice orientation for blue and yellow lined regions, respectively and (i) their FFT pattern. Inverse FFT pattern by point mask mode and their phase profile spectrum for (j−k) 011 and (l−m) 100 orientation.

Heyrovsky process (ion and atom reactions): $H_{ads} + H_3O^+ + e^- \rightarrow H_2 + H_2O$ (40 mV/dec),   (2)

and

Tafel process (combination reaction): $H_{ads} + H_{ads} \rightarrow H_2$ (30 mV/dec)   (3)

Fig. 6 − Morphological studies of PtTe$_2$ (a−c) Low and high magnification FESEM images (d−f) Low and higher magnification TEM images (inset − corresponding FFT pattern) (g−h) High resolution TEM images with different shape of nano-stripe structured fringes and their magnified parts are provided in the circle shape (inset − FFT pattern); (i) Phase profile spectrum for 011 lattice orientation.

Thus, our purposed electrocatalysts (PtS$_2$, PtSe$_2$ and PtTe$_2$) can be obeyed by the Volmer-Heyrovsky mechanism for H$_2$SO$_4$ medium, whereas discharge reaction is a rate-limiting process [15,53]. The extracted Tafel slope and j$_0$ values of PtTe$_2$ are compared with different LTMDs based HER catalysts in Table S1.

To further evaluate the electron-transfer kinetics and the inherent catalytic activity of HER reaction in H$_2$SO$_4$ medium, an electrochemical impedance spectroscopy (EIS) was performed (Fig. 7d). The interactions between the catalyst and the electrolyte interface was determined thru the charge transfer resistance (R$_{ct}$) of electrocatalyst and its low value produces the fast electron transfer. A PtTe$_2$ catalyst exhibits a substantially lower R$_{ct}$ of ~10.23 Ω than the PtS$_2$ and the PtSe$_2$ catalysts (~11.02 & 15.3 Ω). The high HER activity observed in the 1 T-PtTe$_2$ phase is credited to the high conductivity of the metallic nature, which supports the rapid electron transfer within the electrode/electrolyte interface. The small series resistance of ~1.3−2 Ω (Fig. 7d) revealed the strong adherence of Pt-chalcogenides with the high conductive Ti substrate and solid electron coupling effect to minimize the ohmic losses, which explored the significant role of synthetic processes.

The extraction of electrochemical active surface area (ECSA) is a valid tool to assess the electrocatalyst behavior. CVs performance with various scan rates were employed in a non-Faradaic region to perceive the electrochemical double-layer capacitances (C$_{dl}$). Fig. S5 shows the CV curves of the PtS$_2$, PtSe$_2$, and the PtTe$_2$ electrocatalysts for H$_2$SO$_4$ medium. The plotted current differences at 0.125 V vs RHE ($\Delta j = j_{anodic}$-$j_{cathodic}$) against the different scan rates were linearly fitted to evaluate the slope value, which was used as C$_{dl}$ [45,52]. The C$_{dl}$ values were 2.59 mF/cm^2, 2.73 mF/cm^2, and 2.81 mF/cm^2 for the PtS$_2$, PtSe$_2$, and the PtTe$_2$, respectively in acidic medium. The appraised ECSA values were 74 cm^2, 78 cm^2, and 80 cm^2 for the PtS$_2$, PtSe$_2$, and the PtTe$_2$, respectively. This result revealed that PtSe$_2$ and PtTe$_2$ are having the maximum effective active area for high HER reaction kinetics rather than a PtS$_2$ catalyst, which might be originated from the plenty of active sites and the metallic nature of materials. From the observed results, the exhibited excellent morphological properties with the high-density active edge sites for Pt-chalcogenides were highly influenced to achieve the improved electrocatalytic properties. The EIS results were also
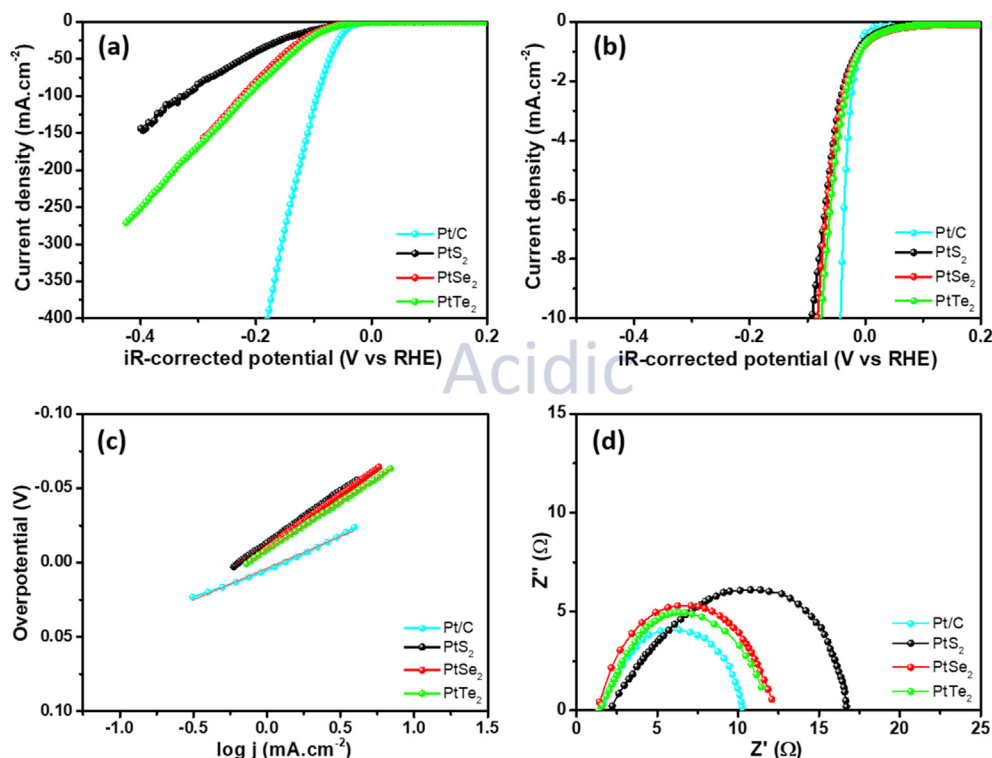
Fig. 7 – Electrocatalytic HER activity of Pt/C, PtS₂, PtSe₂, and PtTe₂ in acidic medium (a–b) LSV curves, (c) Tafel plots, and (d) Nyquist plots.

Table 1 – Comparison of HER activity of Pt-based electrocatalysts.

Electrolyte	Electrocatalysts	Overpotential (mV vs RHE) @ 10 mA cm⁻²	Tafel slope (mV·dec⁻¹)	Exchange current density (j_o, mA·cm⁻²)
0.5 M H₂SO₄	Pt/C	43	42	1.31
	PtS₂	92	69	0.65
	PtSe₂	81	71	0.73
	PtTe₂	75	64	0.77
1 M KOH	Pt/C	42	48	1.17
	PtS₂	95	90	1.08
	PtSe₂	94	78	1.22
	PtTe₂	92	59	0.81

evidently derived the rapid electron transfer and the reaction kinetics of HER for Pt-chalcogenides.

Apart from the high activity of electrocatalysts, the stability is an important criterion to use in the practical applications of HER. The PtS₂, PtSe₂, and PtTe₂ catalysts were used to perform the chronoamperometric (i-t) measurements for a 20 h continuous HER operation with 92, 81, and 75 mV overpotential of PtS₂, PtSe₂, and PtTe₂, respectively, in an acidic solution. Fig. 8a-b shows the i-t curve for the PtS₂ and PtSe₂ catalysts. The observed profiles revealed the substantial degradation for the 20 h continuous HER operation which might be due to the adsorption of H₂ bubbles on the electrode surface to diminish the active sites for the long time performance. The robust behavior is clearly visualized for PtTe₂ catalyst in Fig. 8c, which is credited to the metallic nature of 1 T- PtTe₂. The observed LSV profiles after 20 h HER operation are inserted with the corresponding i-t profile in Fig. 8. Also, the observed LSV profile of PtTe₂ after 20 h HER operation

produces the identical curve with an initial one which further proves the reusable properties.

Furthermore, the SEM results were perceived after a 20 h HER operation for PtS₂, PtSe₂, and PtTe₂ to prove the stable nature of electrocatalysts as shown in Fig. S6. Slightly changed morphologies are observed for PtS₂, PtSe₂, and PtTe₂ compared to before the HER operation due to the 20 h' continuous performance in an acidic electrolyte. However, the shape of the grains is somewhat maintained for the PtTe₂ due to its robust nature in the acidic electrolyte. Besides, the XPS spectra for the PtTe₂ after the 20 h HER operation revealed no noticeable chemical state changes in the electrode surface due to the robust behavior (Fig. S7).

Furthermore, to explore the characteristics of Pt/C, PtS₂, PtSe₂, and PtTe₂ electrocatalysts in the alkaline medium (1 M KOH), LSV profiles were recorded at 10 mV s⁻¹ scan rate. Fig. 9a-b shows the LSV profiles of different electrocatalysts in alkaline medium. The observed overpotentials are 42, 95, 94

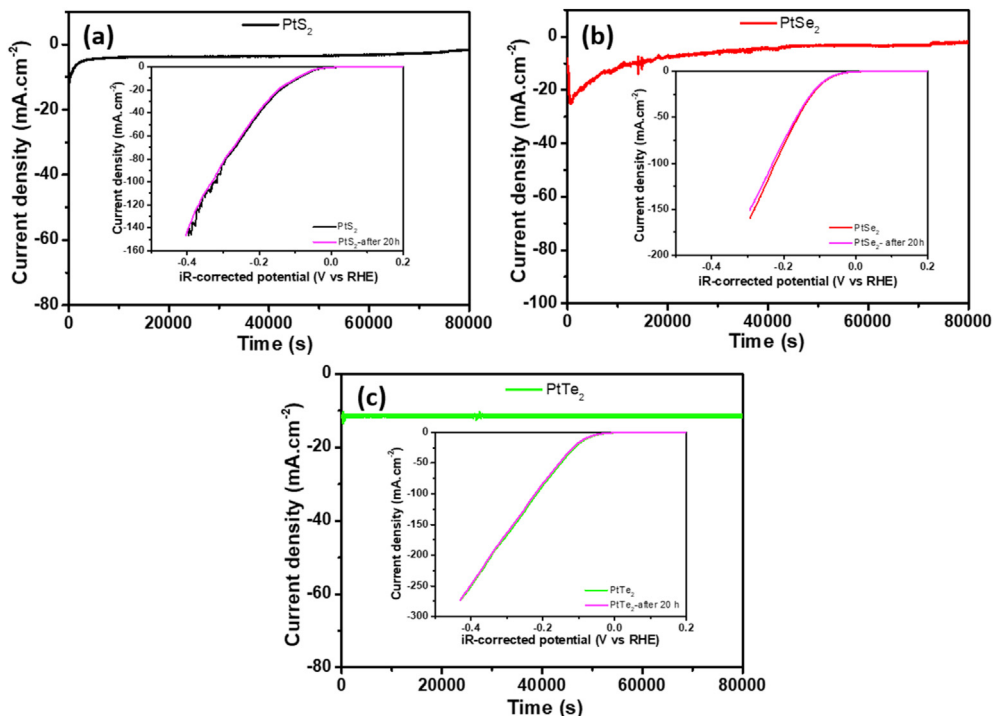**Fig. 8 — Chronoamperometry curves for (a) PtS₂, (b) PtSe₂, and (c) PtTe₂ at 92, 81 & 75 mV vs RHE, respectively (inset - initial and after 20 h HER process obtained LSV curves) in acidic solution.**

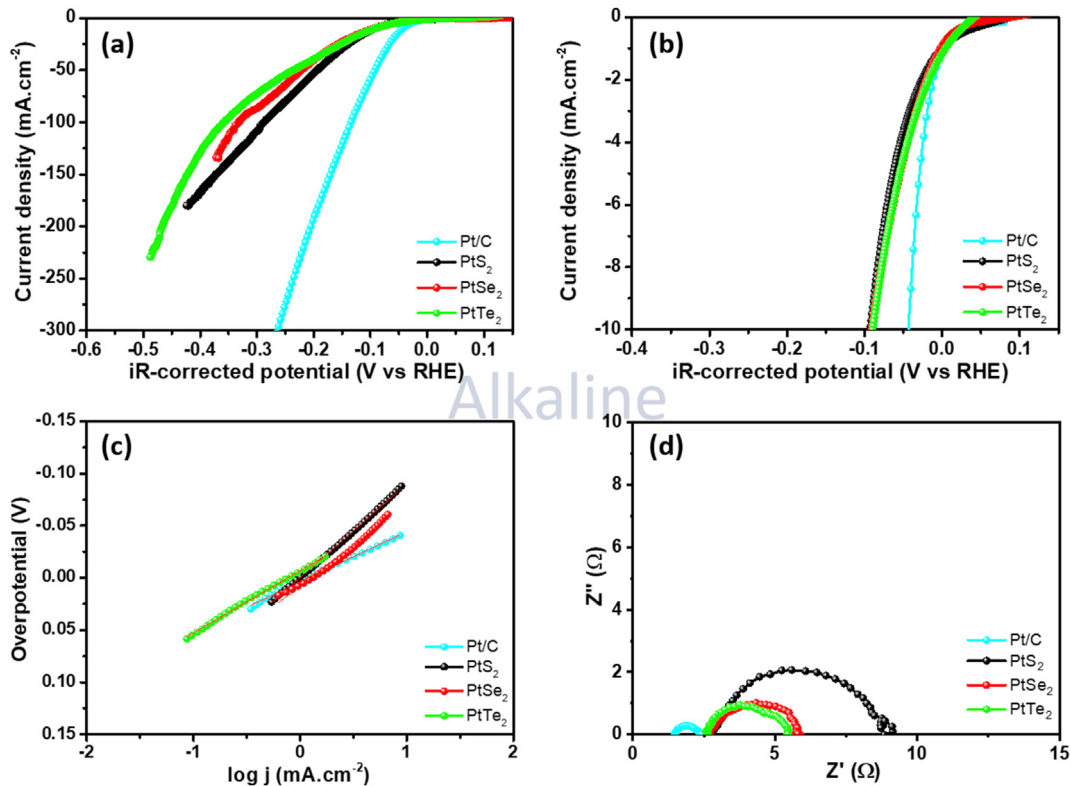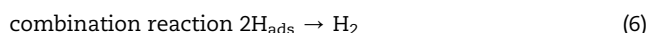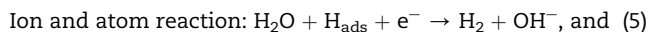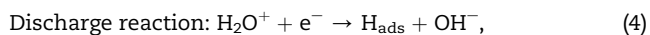**Fig. 9 — Electrocatalytic HER activity of Pt/C, PtS₂, PtSe₂, and PtTe₂ electrocatalysts in alkaline medium (a−b) LSV curves, (c) Tafel plots, and (d) Nyquist plots.**

and 92 mV vs RHE to drive 10 mA cm^{-2} for Pt/C, PtS$_2$, PtSe$_2$, and PtTe$_2$ electrocatalysts, respectively. From the outcomes, PtTe$_2$ catalyst shows the better catalytic activity in the acidic medium than the alkaline medium. Fig. 9c shows the Tafel plots for the Pt/C, PtS$_2$, PtSe$_2$, and the PtTe$_2$ electrodes for alkaline medium. A commercial Pt/C exhibits the 48 mV/dec of Tafel slope value. The PtTe$_2$ electrode shows a minimum Tafel slope of 59 mV/dec (PtSe$_2$: 78 mV/dec, PtS$_2$:90 mV/dec). Three primary HER kinetic steps in alkaline media is described as follows, [5,24].

Discharge reaction: $H_2O^+ + e^- \rightarrow H_{ads} + OH^-$,   (4)

Ion and atom reaction: $H_2O + H_{ads} + e^- \rightarrow H_2 + OH^-$, and (5)

combination reaction $2H_{ads} \rightarrow H_2$ (6)

However, the observed Tafel slopes of PtS$_2$, PtSe$_2$ and PtTe$_2$ indicate that the HER obeys the Volmer−Heyrovsky kinetics in alkaline solution, thus identifying the electrochemical discharge reaction as the rate-limiting process [54,55]. The assessed j_0 values are 1.17, 1.08, 1.22, and 0.81 mA cm^{-2} for Pt/C, PtS$_2$, PtSe$_2$, and the PtTe$_2$, respectively, in the alkaline medium. The exhibited low overpotential and small Tafel slope values for the PtTe$_2$ specifies its rapid reaction kinetics and the superior electrocatalytic HER activity as compared with other Pt-based electrocatalysts due to its metallic nature [15,20,56]. EIS plots were recorded for Pt/C, PtS$_2$, PtSe$_2$, and the PtTe$_2$ electrocatalysts in alkaline medium, as shown in Fig. 9d. The

observation of small Rct characteristics proves the swift electron interactions between the catalyst and the electrolyte interface for H$^+$ reduction in an alkaline medium. A 1 T-PtTe$_2$ catalyst exhibits a substantially small Rct of ~2.6 Ω (PtS$_2$ and PtSe$_2$ catalysts, ~3.2 & 6.1 Ω). The low series resistance of ~2.6−2.8 Ω for the Pt-chalcogenides revealed a high conductive behavior of prepared electrocatalysts. The observed HER parameters for alkaline media are provided in Table 1. Furthermore, an overpotential of PtTe$_2$ catalyst of 92 mV vs RHE was used to derive i-t profile in alkaline medium to prove the stability (Fig. S8). The persistent i-t profile shows for PtTe$_2$ with no negligible decay in current density over the duration of 20 h due to the strong electrocatalytic behavior of electrode. The strong interaction between substrate and PtTe$_2$ nanosheets facilitates the swift transfer of ion/electrons and enables the strong mechanical adhesion boosting the remarkable stability. The fabricated PtS$_2$, PtSe$_2$ and PtTe$_2$ electrocatalysts produced the superior HER behavior in the acidic medium rather than the alkaline medium.

Figs. S9a−f show the optimized chemical structure of the Pt-chalcogenides (PtX$_2$ = PtTe$_2$, PtSe$_2$, and PtS$_2$) bulk phase top and side view. The various optimized lattice parameters are presented in Table S2. The band structure for bulk PtS$_2$, PtSe$_2$, and PtTe$_2$ are shown in Figs. S10a−c. It illustrated that PtS$_2$ and PtSe$_2$ exhibit a semiconductor character with a 1.42 and a 0.66 eV bandgap, respectively. The PtTe$_2$ has a metallic character, so these findings are fairly consistent with the reported outcomes and confirmed the stability of our structures [57]. Then, it assumed the intercalation of H atom on the surface
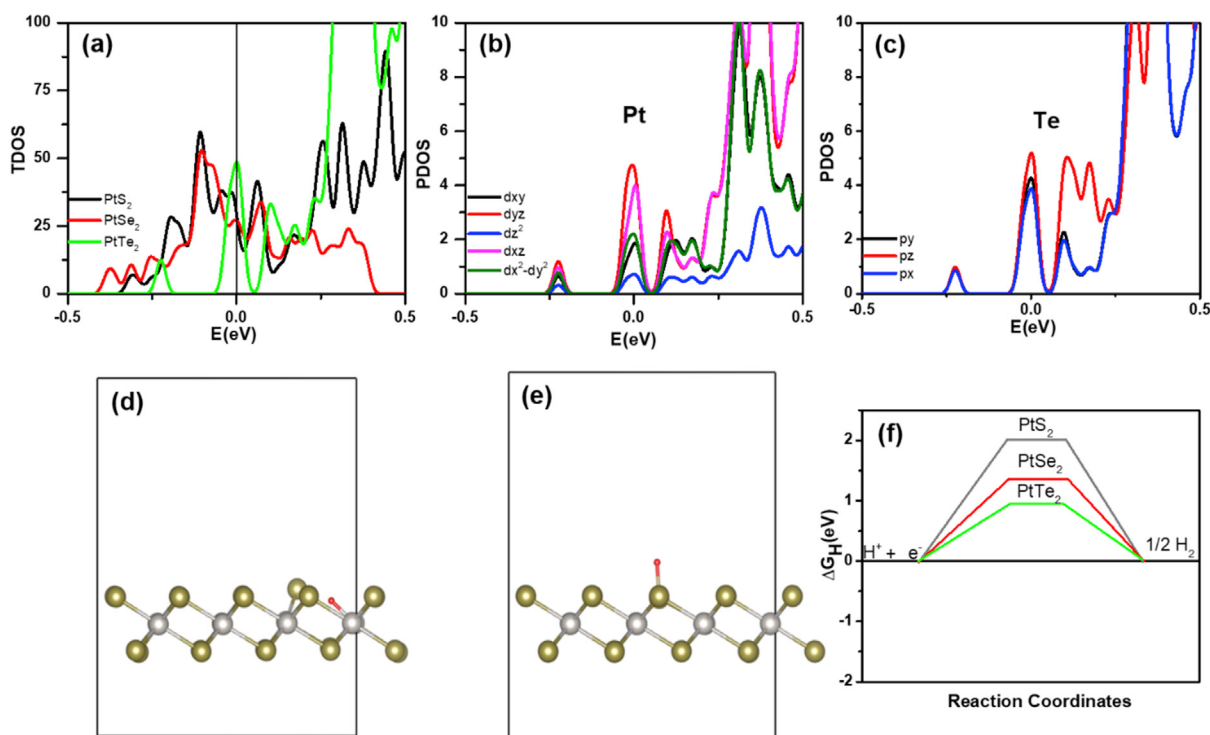
Fig. 10 − (a) The TDOS for hydrogen atom adsorbed PtS$_2$, PtSe$_2$, and PtTe$_2$ (b−c) PDOS for hydrogen atom adsorbed Pt and Te atom in PtTe$_2$. Chemical structure of an H atom adsorbed onto the (d) edge and (e) surface sites in PtX$_2$. (f) Gibbs free energy for hydrogen atom adsorption for PtS$_2$, PtSe$_2$, and PtTe$_2$.

and the edge sites of PtX_2 and derived their relative energy with respect to the most stable configuration. Table S2 shows the adsorption (E_{ad}) and the relative (E_{rel}) energy of a hydrogen atom adsorbed onto the surface and edge sites, and it confirmed that the adsorption of H atom is more favorable to the edge sites of PtX_2. The X—H (X = S, Se, Te) bond lengths are 1.36 Å for PtS_2, 1.49 Å for $PtSe_2$, and 1.72 Å for $PtTe_2$, and they are very close to the hydrides bond lengths (1.30, 1.45, and 1.72 Å for H_2S, H_2Se, and H_2Te, respectively) [58]. Fig. 10a displays the total electronic density of states (TDOS) for the hydrogen atom adsorbed PtX_2 around the Fermi level, and it follows the following order: $PtTe_2 > PtSe_2 > PtS_2$, which indicates that the TDOS is significantly enhanced at the Fermi level when the hydrogen atom adsorbed. Interestingly, the extracted TDOS pattern revealed that the electronic structure of the PtS_2 and $PtSe_2$ were transformed from the semiconductor to the metallic nature. The enhanced partial electronic density of states (PDOS) of $PtTe_2$ was observed around the Fermi level due to the hybridization of dyz (Pt), dxz (Pt), py (Te), pz (Te), and px (Te) states (Fig. 10b-c). Therefore, the transfer of charge from the adsorbed H atom gives a significant part in the increased carrier concentration, the conductivity, and the electron mobility, which is accountable for the enriched HER activity.

In order to realize this output, the change of electron density (e Å^{-3}) is described beside the c axis as $\Delta\rho(z) = \{\rho(z)[PtX_2\text{-}mH] - \rho(z)[PtX_2] - \rho(z)[mH]\}$. Here, $\rho(z)$ signifies that the considered structure electron density is defined in the parentheses, and it is the median of the supercell XY plane. These values were estimated by the subtraction of pristine $PtTe_2$ crystal and H electron density from the H atom adsorbed PtX_2 complex in the same supercell configuration. Note that the total charge is zero for the complex, even though H can occur in the form of H$^+$ ions after the complex creation. Fig. S11a shows $\Delta q(z)$ and $\Delta Q(e)$ of the $PtTe_2$-mH (4 × 4 unit cells) complex. Here, $\Delta\rho(z) = \Delta V\Delta q(z)$, $\Delta V = V_{cell}/N_c$, and N_c (= 216) and V_{cell} are the c-axis number of the fine grids and the volume of the supercell, respectively. Each $PtTe_2$ layer thick is described by the z coordinates of Te atoms of lower (Te_L) and upper sublayers (Te_U), which is z (Te_L) < z (Te_U). In every structure, the thickness of the H$^+$ ions adsorbed $PtTe_2$ is estimated from the difference of the z coordinates minimum and maximum for all the atoms in the unit cell. Furthermore, the $\Delta q(z)$ of the H atom substantially is decreased, which notified the alteration of H atom to the H$^+$ ion and transported the charge to the adjacent Te atoms.

For the quantitative analysis, the gathered excess charge Q(e) is described as $Q(e) = \sum_{0}^{z' < z} \Delta\rho(z')$. Then, the charge transfer amount is clarified by the equation, $\Delta Q(e) = [Q_{max}(z) - Q_{min}(z)]$. From Fig. S11a, $Q_{min}(z)$ and $Q_{max}(z)$ relate to minima and maxima, respectively, which is nearby $PtTe_2$. Hence, the 0.09e$^-$ charge transferred from the adsorbed H to the Te atom. Similarly, Fig. S11b shows the profile images of $\Delta\rho(x, y, z)$ to expose the noteworthy electron transferal from the H atom to the $PtTe_2$ layer. The charge depletion and accumulation are denoted by the green and the red colors, respectively. Transported electrons are gathered between the H and the adjacent Te.

Fig. 10d-e shows the chemical structure of an H atom adsorbed on the surface and on the edge site of PtX_2 for the HER catalytic activity. The DFT calculations derive the $\triangle G_H*$ of H adsorption for PtX_2 (S, Se and Te), which is shown in Fig. 10f. In general, it is necessary to be close to null for the conjucture value of $\triangle G_H*$ for a worthy HER activity, which is an ultimate state to attach the H atom neither too faintly nor too sturdily. With thermodynamics, the H_2 generation is too tricky for too positive adsorption energy of an H atom and to be declined for too negative adsorption energy of an H atom [52,59]. The observed results exposed that $\triangle G_H*$ of $PtTe_2$ is less compared to the $PtSe_2$ and the PtS_2, which is associated with the weakened interactions between the Pt and the Te atoms due to their metallic behavior and a more thermoneutral behavior. The TDOS calculations also indicated a significantly enhanced TDOS at the Fermi level when the hydrogen atom adsorbed with $PtTe_2$. From the derived estimations, it is concluded that HER activity occurs in the order of $PtS_2 < PtSe_2 < PtTe_2$ in the Pt-chalcogenides. The high electrical conductivity and the abundant catalytic activity sites are also supported to perceive superior HER activity in $PtTe_2$ [60].

4. Conclusions

In this report, we systematically investigated the characteristics of sputtering-CVD prepared PtS_2, $PtSe_2$ and $PtTe_2$ layered materials and employed them as robust and highly active electrocatalysts for HER. The metallic $PtTe_2$ catalyst revealed low overpotentials of 75 and 92 mV (vs. RHE) at a current density of 10 mA cm^{-2}, and small Tafel slopes of 64 and 59 mV/dec in acidic and alkaline medium, respectively. Also, $PtTe_2$ showed a robust nature over a 20 h continuous HER process in an acidic and alkaline medium. The DFT calculations derived the low ΔG_H* for the $PtTe_2$ electrode and proved their excellent electrocatalytic HER activity by TDOS and PDOS estimations. This study offers a promising use for Pt-chalcogenides catalysts to boost the HER activity for green energy applications.

Declaration of Competing Interest

The authors declare that they have no known competing financial interests or personal relationships that could have appeared to influence the work reported in this paper.

Acknowledgements

Appendix A. Supplementary data

Supplementary data to this article can be found online at https://doi.org/10.1016/j.jmrt.2021.02.097.

REFERENCES

[1] Turner JA. Sustainable hydrogen production. Science 2004;305:972.

[2] Vikraman D, Akbar K, Hussain S, Yoo G, Jang JY, Chun SH, et al. Direct synthesis of thickness-tunable MoS_2 quantum dot thin layers: optical, structural and electrical properties and their application to hydrogen evolution. Nano Energy 2017;35:101—14.

[3] Vikraman D, Hussain S, Patil SA, Truong L, Arbab AA, Jeong SH, et al. Engineering $MoSe_2/WS_2$ hybrids to replace the scarce platinum electrode for hydrogen evolution reactions and dye-sensitized solar cells. ACS Appl Mater Interfaces 2021;13:5061—72.

[4] Liu B, Zhao Y-F, Peng H-Q, Zhang Z-Y, Sit C-K, Yuen M-F, et al. Nickel—Cobalt diselenide 3D mesoporous nanosheet networks supported on Ni foam: an all-pH highly efficient integrated electrocatalyst for hydrogen evolution. Adv. Mater. 2017;29:1606521.

[5] Hussain S, Rabani I, Vikraman D, Feroze A, Karuppasamy K, Haq Zu, et al. Hybrid design using carbon nanotubes decorated with Mo_2C and W_2C nanoparticles for supercapacitors and hydrogen evolution reactions. ACS Sustain Chem Eng 2020;8:12248—59.

[6] Yin J, Zhan F, Jiao T, Wang W, Zhang G, Jiao J, et al. Facile preparation of self-assembled MXene@Au@CdS nanocomposite with enhanced photocatalytic hydrogen production activity. Sci China Mater 2020;63:2228—38.

[7] Li K, Jiao T, Xing R, Zou G, Zhou J, Zhang L, et al. Fabrication of tunable hierarchical MXene@ AuNPs nanocomposites constructed by self-reduction reactions with enhanced catalytic performances. Sci China Mater 2018;61:728—36.

[8] Wang R, Yan X, Ge B, Zhou J, Wang M, Zhang L, et al. Facile preparation of self-assembled black phosphorus-dye composite films for chemical gas sensors and surface-enhanced Raman scattering performances. ACS Sustainable Chem Eng 2020;8:4521—36.

[9] Liu Y, Hou C, Jiao T, Song J, Zhang X, Xing R, et al. Self-assembled AgNP-containing nanocomposites constructed by electrospinning as efficient dye photocatalyst materials for wastewater treatment. Nanomaterials 2018;8:35.

[10] Li J-S, Wang Y, Liu C-H, Li S-L, Wang Y-G, Dong L-Z, et al. Coupled molybdenum carbide and reduced graphene oxide electrocatalysts for efficient hydrogen evolution. Nat Commun 2016;7:11204.

[11] Kibsgaard J, Tsai C, Chan K, Benck JD, Nørskov JK, Abild-Pedersen F, et al. Designing an improved transition metal phosphide catalyst for hydrogen evolution using experimental and theoretical trends. Energy Environ Sci 2015;8:3022—9.

[12] Wang C, Sun S, Zhang L, Yin J, Jiao T, Zhang L, et al. Facile preparation and catalytic performance characterization of AuNPs-loaded hierarchical electrospun composite fibers by solvent vapor annealing treatment. Colloids Surf A-Physicochem Eng Aspects 2019;561:283—91.

[13] Hussain S, Rabani I, Vikraman D, Feroze A, Ali M, Seo Y-S, et al. MoS_2@X_2C (X=Mo or W) hybrids for enhanced supercapacitor and hydrogen evolution performances. Chem Eng J 2021;127843.

[14] Xu K, Wang F, Wang Z, Zhan X, Wang Q, Cheng Z, et al. Component-controllable $WS_{2(1-x)}Se_{2x}$ nanotubes for efficient hydrogen evolution reaction. ACS Nano 2014;8:8468—76.

[15] Chia X, Adriano A, Lazar P, Sofer Z, Luxa J, Pumera M. Layered platinum dichalcogenides (PtS_2, $PtSe_2$, and $PtTe_2$) electrocatalysis: monotonic dependence on the chalcogen size. Adv Funct Mater 2016;26:4306—18.

[16] Vikraman D, Hussain S, Karuppasamy K, Feroze A, Kathalingam A, Sanmugam A, et al. Engineering the novel $MoSe_2$-Mo_2C hybrid nanoarray electrodes for energy storage and water splitting applications. Appl Catal B Environ 2020;264:118531.

[17] Iordanidou K, Houssa M, Persson C. Carrier-mediated ferromagnetism in two-dimensional PtS_2. RSC Adv 2020;10:952—7.

[18] Xu H, Guo C, Zhang J, Guo W, Kuo C-N, Lue CS, et al. $PtTe_2$-Based type-II Dirac semimetal and its van der Waals heterostructure for sensitive room temperature terahertz photodetection. Small 2019;15:1903362.

[19] Wang Z, Li Q, Besenbacher F, Dong M. Facile synthesis of single crystal $PtSe_2$ nanosheets for nanoscale electronics. Adv. Mater. 2016;28:10224—9.

[20] Wang Y, Li L, Yao W, Song S, Sun J, Pan J, et al. Monolayer $PtSe_2$, a new semiconducting transition-metal-dichalcogenide, epitaxially grown by direct selenization of Pt. Nano Lett 2015;15:4013—8.

[21] Zeng L, Lin S, Lou Z, Yuan H, Long H, Li Y, et al. Ultrafast and sensitive photodetector based on a $PtSe_2$/silicon nanowire array heterojunction with a multiband spectral response from 200 to 1550 nm. NPG Asia Mater 2018;10:352.

[22] Cook TR, Dogutan DK, Reece SY, Surendranath Y, Teets TS, Nocera DG. Solar energy supply and storage for the legacy and nonlegacy worlds. Chem Rev 2010;110:6474—502.

[23] Vikraman D, Hussain S, Truong L, Karuppasamy K, Kim HJ, Maiyalagan T, et al. Fabrication of MoS_2/WSe_2 heterostructures as electrocatalyst for enhanced hydrogen evolution reaction. Appl Surf Sci 2019;480:611—20.

[24] Wang X, Zheng B, Yu B, Wang B, Hou W, Zhang W, et al. In situ synthesis of hierarchical $MoSe_2$—$CoSe_2$ nanotubes as an efficient electrocatalyst for the hydrogen evolution reaction in both acidic and alkaline media. J Mater Chem A 2018;6:7842—50.

[25] Hussain S, Vikraman D, Truong L, Akbar K, Rabani I, Kim HS, et al. Facile and cost-effective growth of MoS_2 on 3D porous graphene-coated Ni foam for robust and stable hydrogen evolution reaction. J Alloys Compd 2019;788:267—76.

[26] Vikraman D, Hussain S, Akbar K, Truong L, Kathalingam A, Chun S-H, et al. Improved hydrogen evolution reaction performance using MoS_2—WS_2 heterostructures by physicochemical process. ACS Sustain Chem Eng 2018;6:8400—9.

[27] Hussain S, Akbar K, Vikraman D, Karuppasamy K, Kim HS, Chun SH, et al. Synthesis of $MoS_{2(1-x)}Se_{2x}$ and $WS_{2(1-x)}Se_{2x}$ alloys for enhanced hydrogen evolution reaction performance. Inorg. Chem. Front. 2017;4:2068—74.

[28] Politano A, Chiarello G, Kuo CN, Lue CS, Edla R, Torelli P, et al. Tailoring the surface chemical reactivity of transition-metal dichalcogenide $PtTe_2$ crystals. Adv Funct Mater 2018;28:1706504.

[29] Rosli NF, Mayorga-Martinez CC, Latiff NM, Rohaizad N, Sofer Zk, Fisher AC, et al. Layered $PtTe_2$ matches electrocatalytic performance of Pt/C for oxygen reduction reaction with significantly lower toxicity. ACS Sustain Chem Eng 2018;6:7432—41.

[30] Shi J, Huan Y, Hong M, Xu R, Yang P, Zhang Z, et al. Chemical vapor deposition grown large-scale Atomically thin platinum diselenide with semimetal—semiconductor transition. ACS Nano 2019;13:8442—51.

[31] Li L, Wang W, Chai Y, Li H, Tian M, Zhai T. Few-layered PtS$_2$ phototransistor on h-BN with high gain. Adv Funct Mater 2017;27:1701011.

[32] Zhao Y, Qiao J, Yu P, Hu Z, Lin Z, Lau SP, et al. Extraordinarily strong interlayer interaction in 2D layered PtS$_2$. Adv. Mater. 2016;28:2399−407.

[33] O'Brien M, McEvoy N, Motta C, Zheng J-Y, Berner NC, Kotakoski J, et al. Raman characterization of platinum diselenide thin films. 2D Mater 2016;3:21004.

[34] Yan M, Huang H, Zhang K, Wang E, Yao W, Deng K, et al. Lorentz-violating type-II Dirac fermions in transition metal dichalcogenide PtTe$_2$. Nat Commun 2017;8:257.

[35] Glamazda A, Choi K, Lemmens P, Yang J, Cheong S. Proximity to a commensurate charge modulation in IrTe$_{2-x}$Se$_x$ (x= 0 and 0.45) revealed by Raman spectroscopy. New J Phys 2014;16:93061.

[36] Yuan J, Sun T, Hu Z, Yu W, Ma W, Zhang K, et al. Wafer-scale fabrication of two-dimensional PtS$_2$/PtSe$_2$ heterojunctions for efficient and broad band photodetection. ACS Appl Mater Interfaces 2018;10:40614−22.

[37] Liu K, Zheng B, Wu J, Chen Y, Wang X, Qi F, et al. Synthesis of two-dimensional semiconductor single-crystal PtSe$_2$ under high pressure. J Mater Sci 2018;53:1256−63.

[38] Yang S, Cai H, Chen B, Ko C, Özçelik VO, Ogletree DF, et al. Environmental stability of 2D anisotropic tellurium containing nanomaterials: anisotropic to isotropic transition. Nanoscale 2017;9:12288−94.

[39] Gao M-R, Liang J-X, Zheng Y-R, Xu Y-F, Jiang J, Gao Q, et al. An efficient molybdenum disulfide/cobalt diselenide hybrid catalyst for electrochemical hydrogen generation. Nat Commun 2015;6:5982.

[40] Konkena B, Masa J, Xia W, Muhler M, Schuhmann W. MoSSe@reduced graphene oxide nanocomposite heterostructures as efficient and stable electrocatalysts for the hydrogen evolution reaction. Nano Energy 2016;29:46−53.

[41] Zhou H, Yu F, Sun J, Zhu H, Mishra IK, Chen S, et al. Highly efficient hydrogen evolution from edge-oriented WS$_{2(1-x)}$Se$_{2x}$ particles on three-dimensional porous NiSe$_2$ foam. Nano Lett 2016;16:7604−9.

[42] Wang F, Li J, Wang F, Shifa TA, Cheng Z, Wang Z, et al. Enhanced electrochemical H$_2$ evolution by few-layered metallic WS$_{2(1-x)}$Se$_{2x}$ nanoribbons. Adv Funct Mater 2015;25:6077−83.

[43] Zhou H, Yu F, Huang Y, Sun J, Zhu Z, Nielsen RJ, et al. Efficient hydrogen evolution by ternary molybdenum sulfoselenide particles on self-standing porous nickel diselenide foam. Nat Commun 2016;7:12765.

[44] Hussain S, Akbar K, Vikraman D, Afzal RA, Song W, An KS, et al. WS$_{(1-x)}$Se$_x$ nanoparticles decorated three-dimensional graphene on nickel foam: a robust and highly efficient electrocatalyst for the hydrogen evolution reaction. Nanomaterials 2018;8:929.

[45] Hussain S, Akbar K, Vikraman D, Liu H, Chun SH, Jung J. WS$_2$/CoSe$_2$ heterostructure: a designed structure as catalysts for enhanced hydrogen evolution performance. J Ind Eng Chem 2018;65:167−74.

[46] Zhuo J, Cabán-Acevedo M, Liang H, Samad L, Ding Q, Fu Y, et al. High-performance electrocatalysis for hydrogen evolution reaction using Se-doped pyrite-phase nickel diphosphide nanostructures. ACS Catal 2015;5:6355−61.

[47] Liu Z, Gao Z, Liu Y, Xia M, Wang R, Li N. Heterogeneous nanostructure based on 1T-phase MoS$_2$ for enhanced electrocatalytic hydrogen evolution. ACS Appl Mater Interfaces 2017;9:25291−7.

[48] Seok J, Lee J-H, Cho S, Ji B, Kim HW, Kwon M, et al. Active hydrogen evolution through lattice distortion in metallic MoTe$_2$. 2D Mater 2017;4:25061.

[49] Bhat KS, Barshilia HC, Nagaraja H. Porous nickel telluride nanostructures as bifunctional electrocatalyst towards hydrogen and oxygen evolution reaction. Int J Hydrogen Energy 2017;42:24645−55.

[50] Luo P, Zhang H, Liu L, Zhang Y, Deng J, Xu C, et al. Targeted synthesis of unique nickel sulfide (NiS, NiS$_2$) microarchitectures and the applications for the enhanced water splitting system. ACS Appl Mater Interfaces 2017;9:2500−8.

[51] Shi Y, Zhou Y, Yang D-R, Xu W-X, Wang C, Wang F-B, et al. Energy level engineering of MoS$_2$ by transition-metal doping for accelerating hydrogen evolution reaction. J Am Chem Soc 2017;139:15479−85.

[52] Vikraman D, Hussain S, Akbar K, Karuppasamy K, Chun SH, Jung J, et al. Design of basal plane edges in metal-doped nanostripes-structured MoSe$_2$ atomic layers to enhance hydrogen evolution reaction activity. ACS Sustain Chem Eng 2019;7:458−69.

[53] Xie J, Zhang H, Li S, Wang R, Sun X, Zhou M, et al. Defect-rich MoS$_2$ ultrathin nanosheets with additional active edge sites for enhanced electrocatalytic hydrogen evolution. Adv. Mater. 2013;25:5807−13.

[54] Hussain S, Rabani I, Vikraman D, Feroze A, Ali M, Seo Y-S, et al. One-pot synthesis of W$_2$C/WS$_2$ hybrid nanostructures for improved hydrogen evolution reactions and supercapacitors. Nanomaterials 2020;10:1597.

[55] Hussain S, Vikraman D, Feroze A, Song W, An K-S, Kim H-S, et al. Synthesis of Mo$_2$C and W$_2$C nanoparticle electrocatalysts for the efficient hydrogen evolution reaction in alkali and acid electrolytes. Front. Chem. 2019;7:716.

[56] Miró P, Ghorbani-Asl M, Heine T. Two dimensional materials beyond MoS$_2$: noble-transition-metal dichalcogenides. Angew Chem Int Ed 2014;53:3015−8.

[57] Guo G, Liang W. The electronic structures of platinum dichalcogenides: PtS$_2$, PtSe$_2$ and PtTe$_2$. J Phys C Solid State Phys 1986;19:995−1008.

[58] Prakash S, Tuli G, Basu S, Madan R. Advanced inorganic chemistry vol, II. New Delhi, India: S. Chand & Co., Ltd 1998;2005:2.

[59] Xing J, Jiang HB, Chen JF, Li YH, Wu L, Yang S, et al. Active sites on hydrogen evolution photocatalyst. J Mater Chem A 2013;1:15258−64.

[60] Liu Y, Wu J, Hackenberg KP, Zhang J, Wang YM, Yang Y, et al. Self-optimizing, highly surface-active layered metal dichalcogenide catalysts for hydrogen evolution. Nat. Energy 2017;2:17127.